Modulation of mechanical resonance by chemical potential oscillation in graphene

The Harvard community has made this article openly available. Please share how this access benefits you. Your story matters

Citation	Chen, Changyao, Vikram V. Deshpande, Mikito Koshino, Sunwoo Lee, Alexander Gondarenko, Allan H. MacDonald, Philip Kim, and James Hone. 2015. "Modulation of Mechanical Resonance by Chemical Potential Oscillation in Graphene." Nature Physics 12 (3) (December 7): 240–244. doi:10.1038/nphys3576.
Published Version	doi:10.1038/nphys3576
Citable link	http://nrs.harvard.edu/urn-3:HUL.InstRepos:34309591
Terms of Use	This article was downloaded from Harvard University's DASH repository, and is made available under the terms and conditions applicable to Other Posted Material, as set forth at http://nrs.harvard.edu/urn-3:HUL.InstRepos:dash.current.terms-of-use#LAA

Modulation of mechanical resonance by chemical potential oscillation in graphene

Changyao Chen[1†], Vikram V. Deshpande[2], Mikito Koshino[3], Sunwoo Lee[4], Alexander Gondarenko[1], Allan H. MacDonald[5], Philip Kim[6] & James Hone[1*]

[1] *Department of Mechanical Engineering, Columbia University, New York, NY 10027, USA*

[2] *Department of Physics and Astronomy, University of Utah, Salt Lake City, UT, 84112, USA*

[3] *Department of Physics, Tohoku University, Sendai 980-8578, Japan*

[4] *Department of Electrical Engineering, Columbia University, New York, NY 10027, USA*

[5] *Department of Physics, University of Texas, Austin, TX 78712, USA*

[6] *Department of Physics, Harvard University, Cambridge, MA, 02138, USA*

[†] *Current address: Center for Nanoscale Materials, Argonne National Laboratory, Lemont, IL, 60439, USA*

[*] *Corresponding email: jh2228@columbia.edu*

The classical picture of the force on a capacitor assumes a large density of electronic states, such that the electrochemical potential of charges added to the capacitor is given by the external electrostatic potential and the capacitance is determined purely by geometry. Here we consider capacitively driven motion of a nano-mechanical resonator with a low density of states, in which these assumptions can break down. We find three leading-order corrections to the classical picture: the first of is a modulation in the static force due to variation in the internal chemical potential; the second and third are change in static force and dynamic

spring constant due to the rate of change of chemical potential, expressed as the quantum (density of states) capacitance. As a demonstration, we study a capacitively driven graphene mechanical resonators, where the chemical potential is modulated independently of the gate voltage using an applied magnetic field to manipulate the energy of electrons residing in discrete Landau levels. In these devices, we observe large periodic frequency shifts consistent with the three corrections to the classical picture. In devices with extremely low strain and disorder, the first correction term dominates and the resonant frequency closely follows the chemical potential. The theoretical model fits the data with only one adjustable parameter representing disorder-broadening of the Landau levels. The underlying electromechanical coupling mechanism is not limited the particular choice of material, geometry, or mechanism for variation in chemical potential, and can thus be extended to other low-dimensional systems.

The calculation of the force between plates of a parallel-plate capacitor by energy methods is a classic problem that illustrates the importance of correct definition of the system's free energy: considering only the energy stored in the capacitor incorrectly predicts a repulsive force of $\frac{1}{2}\left(\mathrm{d}C/\mathrm{d}z\right)\phi^2$, where C is the capacitance, $\mathrm{d}C/\mathrm{d}z$ is its spatial derivative, and ϕ is the electrostatic potential difference. The correct result (an attractive force $-\frac{1}{2}\left(\mathrm{d}C/\mathrm{d}z\right)\phi^2$) is only obtained when the work done by the battery to maintain constant voltage is taken into account[1]. This result assumes a simple system of metallic capacitors with large density of states (DOS), such that the chemical potential μ is constant and the electrostatic potential is identical to the voltage applied by the battery. This assumption breaks down in nanoscale systems, in which the DOS can be

much smaller and μ is no longer fixed, an effect widely studied in electronic devices[2-7]. However, the role of finite DOS in the force between capacitor plates has not been rigorously investigated. Understanding the corrections to the classical model is of fundamental interest and important for modeling of nano-mechanical systems in the atomically thin limit[8,9]. Here we examine the case of a resonant nano-mechanical device, and show that the first-order correction to the resonant frequency consists of three terms, one proportional to μ and two proportional to its derivative $\mathrm{d}\mu/\mathrm{d}n$, with the latter represented through the inverse quantum capacitance $C_Q^{-1} = \frac{1}{Ae^2}\frac{\mathrm{d}\mu}{\mathrm{d}n}$ (A is the sample size and e is the electron charge). The phenomenon is explored experimentally by examining the behavior of a graphene resonator, in which μ is tuned by a perpendicular magnetic field B at *fixed electrochemical potential*. We observe strong frequency shifts that are periodic in $1/B$, and can be quantitatively described by the theoretical model. We further find that, in the limit of an ultra-clean device with low tension, the first term can provide the dominant tuning effect, demonstrating that a nano-mechanical device can be used to track its own chemical potential.

We model a generic mechanical resonator as a mass on a nonlinear spring, capacitively actuated by a nearby gate electrode, as shown in fig. 1. A direct current (DC) voltage V_g applied to the gate can both increase the resonant frequency by exerting a static force to change the equilibrium deflection z_e, and decrease the frequency due to the nonlinear electrostatic potential, an effect known as electrostatic spring softening[10]. The two effects provide an effective spring constant given by:

$$k_{\mathrm{eff}} = k + \eta\alpha z_e^2 - \frac{1}{2}\frac{\mathrm{d}^2 C_{\mathrm{total}}}{\mathrm{d}z^2}V_g^2, \tag{1}$$

where k is the linear spring constant, α is the elastic nonlinear coefficient, and η is the geometric

coefficient that depends on the exact form of static deflection (see Supplementary Information, section 2). In rigid microelectromechanical devices (MEMS), the last capacitive softening term provides the dominant tuning effect, whereas in atomically thin materials under low tension, the second mechanical stiffening term can dominate.

The role of the finite density of states is modeled by considering the variation in μ with carrier density n, such that the electrostatic potential is given by $\phi = V_g - \mu/e$, and by including C_Q in series with C_g. In this case, we first find that the static capacitive force is given by (Supplementary Information, section 3):

$$F = -\frac{1}{2}\left(V_g - \frac{\mu}{e}\right)^2\left(1 - 2\frac{C_g}{C_Q}\right)\frac{\mathrm{d}C_g}{\mathrm{d}z}. \tag{2}$$

When V_g is kept constant and μ and C_Q are modulated, the change in static force is approximated as:

$$\Delta F \approx -\left[\frac{\Delta\mu}{e} + C_g V_g \Delta\left(\frac{1}{C_Q}\right)\right]V_g\frac{\mathrm{d}C_g}{\mathrm{d}z}. \tag{3}$$

The change in static force shifts the equilibrium deflection z_e, thus the resonant frequency, and alters the curvature of the potential energy at the equilibrium position, as determined from the spatial derivative of ΔF. The leading term in the latter is given by:

$$\Delta k = \frac{\mathrm{d}\Delta F}{\mathrm{d}z} = \left(V_g\frac{\mathrm{d}C_g}{\mathrm{d}z}\right)^2\Delta\left(\frac{1}{C_Q}\right). \tag{4}$$

Combining the effects from eq. (2) and (3), we arrive at the total frequency shift as:

$$\Delta f_{\text{total}} = -\Re_V\left(\frac{\Delta\mu}{e}\right) - \Re_V C_g V_g \Delta\left(\frac{1}{C_Q}\right) + \frac{f_0}{2k_0}\left(V_g\frac{\mathrm{d}C_g}{\mathrm{d}z}\right)^2\Delta\left(\frac{1}{C_Q}\right), \tag{5}$$

where $\Re_V = |\mathrm{d}f_0/\mathrm{d}V_g|$ indicates how easily the resonant frequency f_0 can be tuned by electrostatic potential, k_0 is the unmodulated spring constant, $\Delta\mu$ is change in chemical potential, and $\Delta\left(1/C_Q\right)$

represents the change in inverse quantum capacitance. The three terms in eq. (5) are referred to below as Δf_1, Δf_2, and Δf_3, respectively. Importantly Δf_1 is a direct measure of variation in the chemical potential, whereas Δf_2 and Δf_3 depend on the change in quantum capacitance. We also note that these terms are closely related to experiments with nanotube quantum dot mechanical resonators[8,9], in which $\Delta f_{2,3}$ are analogous to the diverging charge susceptibility of the quantum dot that produces dips in the nanotube mechanical frequency at charge transitions, and Δf_1 plays a similar role that changes the static tension and the mechanical frequency from discretely charging the quantum dot.

We examine this phenomenon experimentally using graphene mechanical resonators[11,12], where a transverse magnetic field B is used to tune μ and C_Q independently of V_g. The samples are in a three-terminal configuration (fig. 2a) with a local gate (LG) placed few hundred nanometers away from the suspended graphene. The graphene is assumed to have built-in strain ε_0 from the fabrication process, with additional strain induced by the DC gate voltage V_g. We use a continuum mechanical model for calculation of $f(V_g)$ at different levels of ε_0 (fig. 2b, also Supplementary Information, section 3). Fig. 2c shows $\Re_V$ as a function of ε_0, at three different values of V_g, for a 2 by 2 μm single layer graphene resonator. Thus, in devices with low ε_0, $\Re_V$ can be large and $\Delta f_{1,2}$ are maximized whereas in devices with large ε_0, $\Re_V$ is substantially smaller and $\Delta f_{1,2}$ should be minimized relative to Δf_3. We note that previous studies of graphene resonators in high magnetic fields[13] utilized samples with high tension and therefore observed only the effects of Δf_3; in the experimental work below, we focus on samples with ultralow tension to directly observe the effects of chemical potential variation.

In a transverse magnetic field, electronic states of graphene form discrete Landau levels (LLs), and μ oscillates in a sawtooth pattern with increasing B. The oscillation in μ is reflected in the longitudinal electrical resistivity[14–16] (Shubnikov-de Haas oscillations), and in the magnetization $M = -\mathrm{d}\mu/\mathrm{d}B$ (de Haas-van Alphen oscillations, typically detected by torque magnetometry[17]), but can also be studied explicitly using a sensitive single-electron transistor electrometer[18, 19]. In a single particle picture, the dependence of μ and C_Q on B is determined by the filling fraction $\nu = 2\pi n\hbar/eB$ ($\hbar$ is the reduced Planck's constant), and disorder. We construct a simple model[20] consisting of up to 20 Gaussian-broadened LLs with disorder-induced width Γ (in units of $v_F\sqrt{2e\hbar B}$, where $v_F = 10^6$ m/s is the Fermi velocity). The DOS is given by $D(E) = \mathrm{d}n/\mathrm{d}\mu \propto \sum\limits^{N} \exp[-(E - E_N)^2/\Gamma^2]$, where E_N is center of the Nth LL. Within each LL, E_N of single-layer graphene evolves with B as $E_N(B) = v_F\,\mathrm{sgn}(N)\sqrt{2e\hbar B|N|}$. Here μ is assigned as the highest filled energy level, and C_Q is defined as $Ae^2D(E)$, where A is the sample area. Figures 2d, 2e and 2f show the simulated $\Delta\mu$ as a function of B and accompanying frequency shifts calculated from each of the terms in eq. (5) for three different combinations of high/low tension and disorder. In the case of low tension but large disorder (fig. 2d), $\Delta f_{1,2,3}$ are all reflected in the total frequency shift, but LL broadening largely obscures the variation in μ. In the case of high tension and small disorder (fig. 2e), we found that $\Delta f_3 > \Delta f_{1,2}$ as expected, leading to sharp spikes in frequency at LL transitions. Finally, in the case of both low tension and low disorder, the frequency shift closely (but not completely) follows the contribution of Δf_1 and the sawtooth variation of μ, with spikes at the transitions between LLs due to $\Delta f_{2,3}$.

This simulation motivates the use of graphene samples with very low built-in strain and

disorder, in order to directly observe variation in μ. To prevent contamination, we prepare samples by direct exfoliation of graphite over pre-patterned electrodes[21], and further clean the graphene by Joule heating in vacuum at low temperature[22,23]. The electronic quality is examined through separate measurements (Supplementary Information, section 1), and can yield charged impurity density as low as $\sim 8 \times 10^9$ cm^{-2}. For mechanical resonance measurements, the graphene is actuated electrostatically by adding a small radiofrequency drive voltage to the gate, and the gate-drain current at the same frequency is read out by a vector network analyzer; on resonance, the changing capacitance due to mechanical motion causes a measurable peak in the current[21,24]. The absence of DC bias avoids Joule heating and possible Lorentz forces. We scan V_g up to ± 10 V at zero magnetic field to determine $\Re_V$ and use the continuum mechanical model to extract ε_0. The use of substrate-fixed electrodes eliminates tensioning due to thermal contraction of the metal[12,25], and we are able to achieve $\Re_V$ as large as 10 MHz/V, with $\varepsilon_0 \sim 10^{-4}$.

Figure 3a shows the response of mechanical resonance to applied magnetic filed B, for device D1 with $\Re_V$ of 2 MHz/V. There is no obvious frequency shift with B, except for regimes between LLs, where sharp spikes are evident but the signal becomes weak. Such observations agree well with the predictions for small $\Re_V$ and experimental results reported by Singh *et al.*[13]. Fig. 3b shows the same measurements on device D2 (length 2.4 μm, width 3.2 μm), with $\Re_V$ of 10 MHz/V. The data reveals a repeated pattern of oscillations that are periodic in $1/B$ (Supplementary Information, section 4), allowing us to directly extract the carrier density n of 2.4×10^{11} cm^{-2}. We use the measured value of n at 5 different values of V_g, combined with finite element simulation (COMSOL Multiphysics) to obtain the effective displacement z_e and dC_g/dz as C_g/z_e as a func-

tion of V_g. Therefore, the only free parameter left to fit eq. (5) is the disorder level Γ, which will determine $\Delta\mu$ and $\Delta(1/C_Q)$. We found that a Γ of 0.1 gives satisfactory result. The corresponding $\mu(B)$, that gives rise to Δf_1, is overlaid as a yellow curve in fig. 3b. For comparison, we also plot $E_N(B)$ for the first five LLs as dotted green lines. We found that μ traces E_N closely in each LL, confirming that the frequency can closely track μ in high quality samples. The detailed fit between the model and the data is shown in fig. 3c. Here, the solid points represent the resonant frequency exctracted at each value of B from the data in fig. 3b, and the line represents the prediction of eq. (5) with $\Gamma = 0.1$. The fit is excellent and validates the model presented above.

We briefly consider the region between LLs, where the frequency shift should be primarily sensitive to C_Q. At high magnetic fields, when the sample enters the well-developed quantum Hall regime, its bulk becomes insulating and the edges host dissipationless one-dimensional edge states. This will not change the static charge on the sample and the static force due to V_g, and therefore first two terms of eq. (5) should be unaffected. However, when the bulk becomes sufficiently insulating such that its RC charging time is greater than the mechanical resonance period, the dynamic charging should be determined by the geometric capacitance between the gate and the edge channels, which can be an order of magnitude smaller than C_g (see Supplementary Information, section 5). This has two consequences. First, both the third term in eq. (5) and the classical electrostatic softening term in eq. (1) should decrease with the decreasing dynamic capacitance; in general, the classical term will dominate and the frequency spike will be larger than predicted by eq. (5). Second, both the radiofrequency drive and capacitive displacement current will also decrease, leading to substantial loss of signal. As a consequence, we can use the loss of signal

8

to directly determine the onset of the bulk insulating behavior. In fig. 3b,c (also see fig. S11), this is seen to occur for the final spike, at the transition between $N = 2$ and $N = 1$, indicated by the dashed line in fig. 3c. For this transition, we expect that the model will not fit the data well, and indeed, the magnitude and width of the frequency spike, where observable, seem to exceed the prediction. Nevertheless, the best fit of the limited data in the region between LLs yields C_Q with values similar to previous measurements of high quality graphene samples[27,28]. More detailed modeling and alternative transduction techniques (*e.g.* optical detection) may allow better study of the detailed behavior between LLs.

Figure 4a shows similar data at different values of V_g, with fits using Γ values within $\pm$ 10%. Since we are able to "read off" chemical potential variation directly through mechanical resonance shifts, we can then track the chemical potential as a function of the filling fraction ν. Fig. 4b shows $\Delta\mu(\nu)$ at four different values of V_g: there are distinct jumps of μ at $\nu = 4(N + 1/2)$, which represent the energy gaps between neighboring LLs. We linearly extrapolate to extract the energy gaps, as plotted in fig 4c. In addition, the same analysis allows extrapolation to determine the chemical potential at zero magnetic field $\mu_0 = \hbar v_F \sqrt{\pi n}$. As shown in fig. 4d, this follows $\sqrt{V_g}$ as expected. Therefore the mechanical measurements can, under appropriate conditions, provide a direct means to monitor the chemical potential evolution of the underlying system, in a straightforward manner. We expect to extend our measurements into extreme quantum regimes at larger B, where additional chemical potential jumps would suggest the formation of many-body incompressible states.

Our nanomechanical technique thus provides access to a key thermodynamic quantity (chemical potential) in a self-contained manner. Specifically, our system allows measurements of both the energy gaps, and the gradual energy transition between gaps, which would otherwise require specialized instrumentation[18,19]. In the future, measurements of other correlation effects like negative compressibility[29,30], fractional quantum Hall effects[19,31–35] and Wigner crystallization[36], all of which have thermodynamic signatures, should be possible using this technique. Finally, we emphasize that the electromechanical mechanism identified in the present work is not specific to graphene. Indeed, any atomically thin mechanical resonator with a quasi-2D electronic structure will demonstrate this sensitive response to external fields via an electrostatically controlled mechanism.

Methods

Device Fabrication High resistivity silicon wafers (>20,000 Ω cm) are used in the experiments described in the main text, in order to minimize the parasitic capacitance in the radio frequency (RF) range. 290 nm of thermal oxide is then grown to have best optical contrast for identifying single layer graphene in later studies.

Source and drain electrodes (1 nm Cr, 15 nm Au) are first patterned by DUV photo-lithography (ASML 300C DUV stepper, Cornell Nanofabrication Facility). Next, a dry etch (CF_4) creates 200 nm deep trenches between source and drain electrodes, and finally local gate electrodes (1 nm Cr, 20 nm Au) are deposited in the trenches with careful alignment. The detail of the fabrication is described elsewhere[24].

Graphene samples are prepared by mechanical exfoliation of Kish graphite. The color contrast of the substrate-supported region aids in identification of thin flakes crossing the electrodes. The precise number of layers is subsequently confirmed by Raman spectroscopy.

Device Characterization Suspended graphene samples are electrically tested at room temperature under vacuum before cool-down. Only samples that possess reasonable transconductance ($\Delta R > 100\Omega$ with in 10 V change of gate voltage) are chosen for further investigation.

For low temperature measurements in a magnetic field, samples are wire-bonded and loaded into a home-built insert for the Quantum Design Physical Properties Measurement System (PPMS, 1.8 K base temperature) with 8 semi-rigid coaxial cables to transmit both DC and RF signals. Most

suspended graphene samples show improved quality (narrower Dirac peak) upon cooling. Sample quality is further improved by gentle current annealing[23]. After such treatments, the smallest full-width at half-maximum (FWHM) of the Dirac peak is about 0.2 V, corresponding to a disorder density of $\sim 8 \times 10^9$ cm^{-2}. To avoid collapsing the graphene due to electrostatic force, we only apply gate voltage within ± 10 V.

References

1. Feynman, R. P., Leighton, R. B. & Sands, M. *The Feynman Lectures on Physics*, vol. 2 (Basic Books, 2013).

2. Klitzing, K. v., Dorda, G. & Pepper, M. New method for high-accuracy determination of the fine-structure constant based on quantized hall resistance. *Phys. Rev. Lett.* **45**, 494–497 (1980).

3. Fulton, T. A. & Dolan, G. J. Observation of single-electron charging effects in small tunnel junctions. *Phys. Rev. Lett.* **59**, 109–112 (1987).

4. Luryi, S. Quantum capacitance devices. *Applied Physics Letters* **52**, 501–503 (1988).

5. Park, J. *et al.* Coulomb blockade and the kondo effect in single-atom transistors. *Nature* **417**, 722–725 (2002).

6. Ilani, S., Donev, L. A., Kindermann, M. & McEuen, P. L. Measurement of the quantum capacitance of interacting electrons in carbon nanotubes. *Nature Physics* **2**, 687–691 (2006).

7. Xia, J., Chen, F., Li, J. & Tao, N. Measurement of the quantum capacitance of graphene. *Nature Nanotech.* **4**, 505–509 (2009).

8. Steele, G. A. *et al.* Strong coupling between single-electron tunneling and nanomechanical motion. *Science* **325**, 1103–1107 (2009).

9. Lassagne, B., Tarakanov, Y., Kinaret, J., Garcia-Sanchez, D. & Bachtold, A. Coupling mechanics to charge transport in carbon nanotube mechanical resonators. *Science* **325**, 1107–1110 (2009).

10. Lifshitz, R. & Cross, M. C. Nonlinear dynamics of nanomechanical and micromechanical resonators. In *Reviews of Nonlinear Dynamics and Complexity*, 1–52 (Wiley-VCH Verlag GmbH & Co. KGaA, 2009).

11. Bunch, J. S. *et al.* Electromechanical resonators from graphene sheets. *Science* **315**, 490–493 (2007).

12. Chen, C. *et al.* Performance of monolayer graphene nanomechanical resonators with electrical readout. *Nature Nanotechnol.* **4**, 861–867 (2009).

13. Singh, V. *et al.* Coupling between quantum hall state and electromechanics in suspended graphene resonator. *Applied Physics Letters* **100**, 233103 (2012).

14. Zhang, Y. B., Tan, Y. W., Stormer, H. L. & Kim, P. Experimental observation of the quantum hall effect and berry's phase in graphene. *Nature* **438**, 201–204 (2005).

15. Novoselov, K. S. *et al.* Two-dimensional gas of massless dirac fermions in graphene. *Nature* **438**, 197–200 (2005).

16. Castro Neto, A. H., Guinea, F., Peres, N. M. R., Novoselov, K. S. & Geim, A. K. The electronic properties of graphene. *Rev. Mod. Phys.* **81**, 109–162 (2009).

17. Eisenstein, J. P. *et al.* Density of states and de haas—van alphen effect in two-dimensional electron systems. *Phys. Rev. Lett.* **55**, 875–878 (1985).

18. Zhitenev, N. B. *et al.* Imaging of localized electronic states in the quantum hall regime. *Nature* **404**, 473–476 (2000).

19. Feldman, B. E., Krauss, B., Smet, J. H. & Yacoby, A. Unconventional sequence of fractional quantum hall states in suspended graphene. *Science* **337**, 1196–1199 (2012).

20. Koshino, M. & Ando, T. Diamagnetism in disordered graphene. *Phys. Rev. B* **75**, 235333 (2007).

21. Xu, Y. *et al.* Radio frequency electrical transduction of graphene mechanical resonators. *Appl. Phys. Lett.* **97**, 243111 (2010).

22. Moser, J., Barreiro, A. & Bachtold, A. Current-induced cleaning of graphene. *Appl. Phys. Lett.* **91**, 163513–163513–3 (2007).

23. Bolotin, K. *et al.* Ultrahigh electron mobility in suspended graphene. *Solid State Communications* **146**, 351–355 (2008).

24. Chen, C. *Graphene NanoElectroMechanical Resonators and Oscillators*. Ph.D. thesis, Columbia University (2013).

25. Singh, V. *et al.* Probing thermal expansion of graphene and modal dispersion at low-temperature using graphene nanoelectromechanical systems resonators. *Nanotechnology* **21**, 165204–165204 (2010).

26. Williams, J. R., Abanin, D. A., DiCarlo, L., Levitov, L. S. & Marcus, C. M. Quantum hall conductance of two-terminal graphene devices. *Phys Rev B* **80**, 045408 (2009).

27. Martin, J. *et al.* The nature of localization in graphene under quantum hall conditions. *Nature Physics* **5**, 669–674 (2009).

28. Yu, G. *et al.* Interaction phenomena in graphene seen through quantum capacitance. *Proceedings of the National Academy of Sciences* **110**, 3282–3286 (2013).

29. Efros, A. Density of states of 2d electron gas and width of the plateau of iqhe. *Solid State Communications* **65**, 1281–1284 (1988).

30. Kravchenko, S. V., Rinberg, D. A., Semenchinsky, S. G. & Pudalov, V. M. Evidence for the influence of electron-electron interaction on the chemical potential of the two-dimensional electron gas. *Phys. Rev. B* **42**, 3741–3744 (1990).

31. Bolotin, K. I., Ghahari, F., Shulman, M. D., Stormer, H. L. & Kim, P. Observation of the fractional quantum hall effect in graphene. *Nature* **462**, 196–199 (2009).

32. Du, X., Skachko, I., Duerr, F., Luican, A. & Andrei, E. Y. Fractional quantum hall effect and insulating phase of dirac electrons in graphene. *Nature* **462**, 192–195 (2009).

33. Dean, C. R. *et al.* Multicomponent fractional quantum hall effect in graphene. *Nature Physics* **7**, 693–696 (2011).

34. Dean, C. *et al.* Hofstadter/'s butterfly and the fractal quantum hall effect in moire superlattices. *Nature* **497**, 598–602 (2013).

35. Ponomarenko, L. *et al.* Cloning of dirac fermions in graphene superlattices. *Nature* **497**, 594–597 (2013).

36. MacDonald, A. H., Oji, H. C. A. & Liu, K. L. Thermodynamic properties of an interacting two-dimensional electron gas in a strong magnetic field. *Phys. Rev. B* **34**, 2681–2689 (1986).

Author Contributions C.C. and V.V.D. fabricated and characterized the samples, developed the measurement technique and performed the experiments, data analysis and theoretical modeling. M.K. performed disorder-broadened calculations. S.L. and A. G. helped in sample fabrication. A. H. M. provided theoretical support. P.K. and J.H. oversaw the project. C.C., V.V.D., P.K. and J.H. co-wrote the paper. All authors discussed and commented on the manuscript.

Figure 1   Mass on a nonlinear spring balanced with electrostatic force. The force exerted by the spring varies nonlinearly with the displacement z, and the electrostatic force is determined not only by gate capacitance C_g, electrostatic potential ϕ, but also quantum capacitance C_Q. For fixed electrochemical potential V_g, ϕ is directly modified by chemical potential μ, therefore the total spring constant k_{total} is modulated by both μ and C_Q, and magnified by the nonlinear effect (large α).

Figure 2   Mechanical resonance modulation. **(a)** Schematic of the graphene mechanical resonator with source (S), drain (D) and local gate (LG) contacts. Scale bar: 1 μm. **(b)** Simulated resonant frequency for a 2 by 2 μm graphene resonator with 120 nm gap, at different initial strain ε_0. **(c)** Calculated $\Re_V$ as function of initial strain ε_0 for single layer graphene resonator, at different gate voltage V_g. The negative $\Re_V$ indicates electrostatic softening effect. **(d)**, **(e)**, **(f)** Simulated frequency shifts under high disorder and large $\Re_V$, **(d)**; low disorder and small $\Re_V$ **(e)**; low disorder and large $\Re_V$ **(f)**. Top panel: μ (to the right) and accompanied frequency oscillation Δf_1 (to the left) as function of magnetic field B. Middle panel: corresponding frequency shifts Δf_2 and Δf_3 (see main text). Bottom panel: the total frequency shift as function of B, with Δf_1 overlaid on top (black), except for **(d)**. For all the simulations, V_g = 10V, ε_0 = 0.01%, Q = 2000, signal-to-noise ratio = 10 dB, f_0 = 161.4 MHz, and f_{min} is 360 Hz assuming 100 Hz measurement bandwidth.

Figure 3   Chemical potential variation induced frequency shifts. **(a)** Measured magnitude of S_{21} transmission as function of applied magnetic field for device D1. Due to the

18

small frequency tunability, there is no obvious mechanical resonance shift within single LL. . Test conditions: T = 4.3 K, V_g = -6 V, drive power is -62 dBm. **(b)** Similar measurement for device D2, which has larger frequency tunability. The corresponding chemical potential variation is overlaid in yellow. The green dotted lines show the LL energies for N = 1 to 5. Test conditions: T = 4.3 K, V_g = -4.2 V, drive power is -68 dBm. **(c)** Complete fitted result (red curve) to the data shown in **(b)**. The dashed line indicates where the model is not expected to be accurate.

Figure 4 Chemical potential evolutions and overall fits to experimental data. **(a)** Mechanical resonant frequency as functions for applied magnetic fields at different V_g, and corresponding fits (red curves). The dashed line for V_g = -3.4 V indicates where the model is not expected to be accurate (see text). **(b)** Extracted chemical potential changes for different V_g, as function of filling factors. The dashed blue line shows the linear extrapolation used to determine the energy gaps at integer filling factors. **(c)** Energy gaps at different integer filling factors for various V_g. **(d)** Chemical potential at zero magnetic field, μ_0 at different V_g. Red solid curve is $\sqrt{V_g}$ fit.

a

S   LG   D
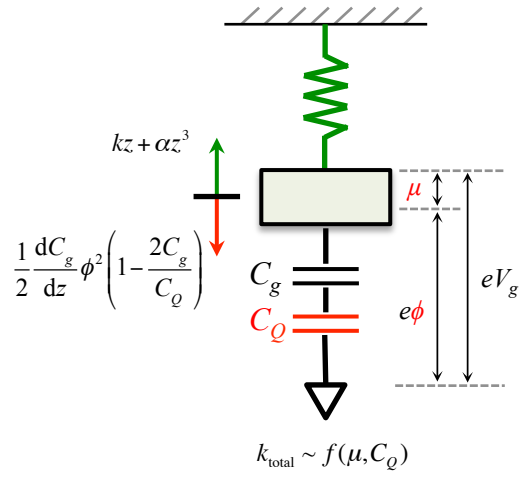
detection

V_g

b

Frequency (MHz)

200

150

100

50

$\varepsilon_0 = 0.1\%$
$\varepsilon_0 = 0.01\%$

-10   -5   0   5   10

V_g (V)

c

R_V (MHz / V)

15

10

5

0

-5

V_g (V)
1
5
10

0.001   0.01   0.1   1

Initial strain ε_0 (%)

d

$\Gamma = 0.25$
$R_V = 11.1$ MHz/V Δf_1

20

0

$\Delta f/\Delta f_{min}$

100
0
-100

Δf_2 Δf_3

10

-10

Δf_{total}

-60

-61

$-\mu$ (meV)

0.5   1   1.5   2   2.5

B (T)

e

$\Gamma = 0.125$
$R_V = 1.1$ MHz/V Δf_1

10

0

$\Delta f/\Delta f_{min}$

3000
1500
0

Δf_2 Δf_3

1000
0

Δf_{total}

-50

-60

-70

$-\mu$ (meV)

0.5   1   1.5   2   2.5

B (T)

f

$\Gamma = 0.125$
$R_V = 11.1$ MHz/V Δf_1

100

0

$\Delta f/\Delta f_{min}$

2000
0
-2000

Δf_3 Δf_2

100
0

Δf_{total}

-50

-60

-70

$-\mu$ (meV)

0.5   1   1.5   2   2.5

B (T)

a

b

c
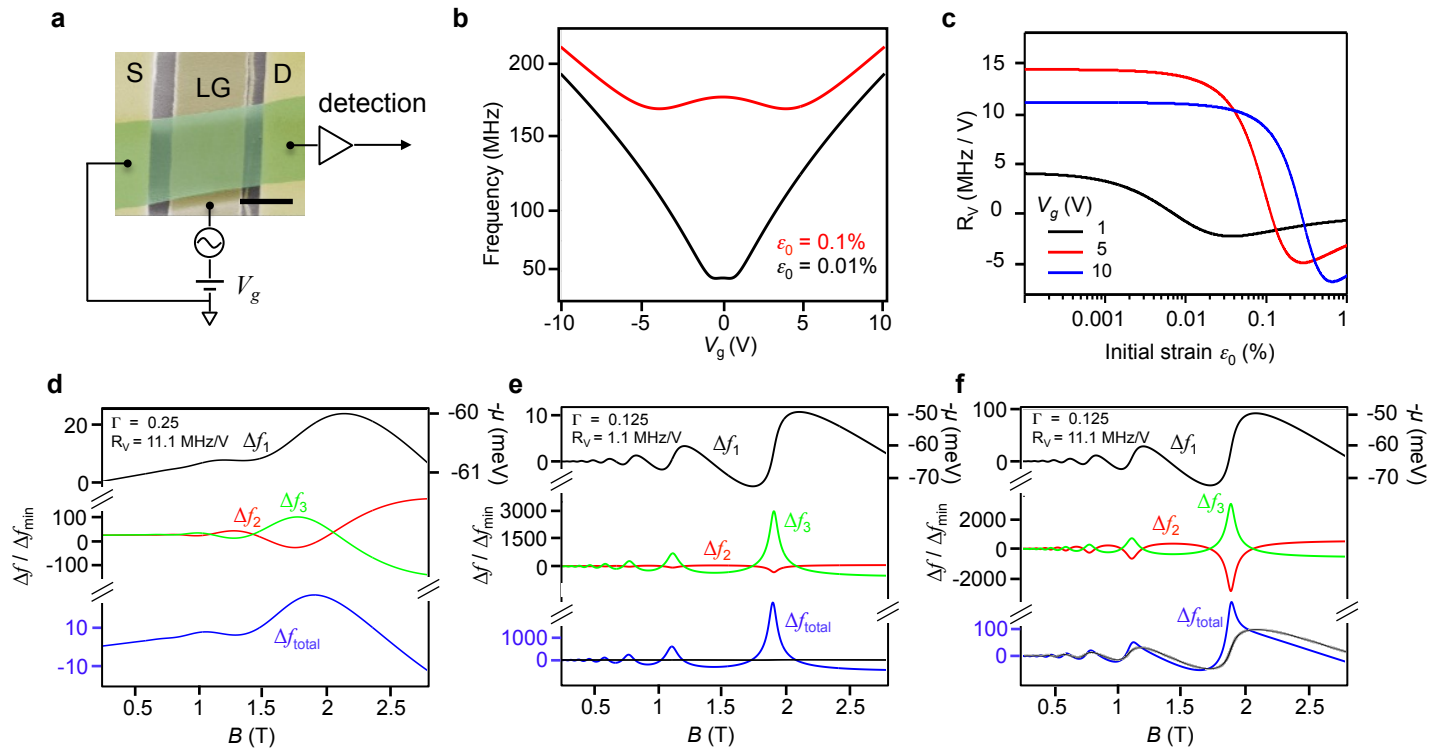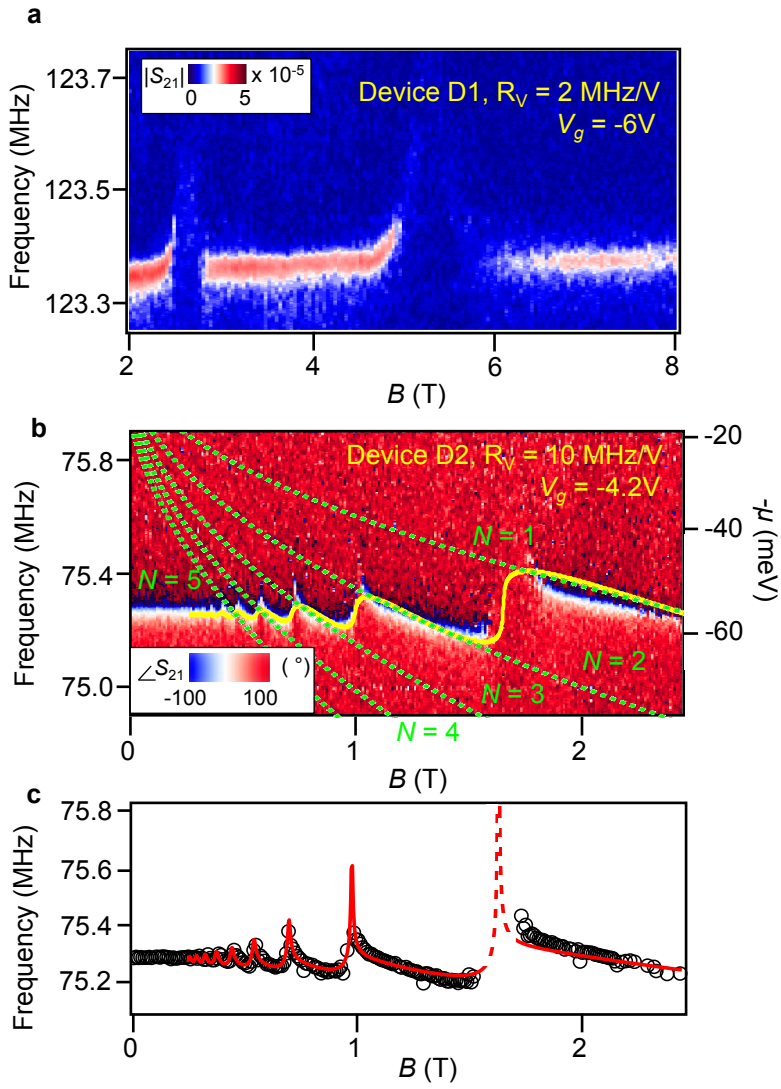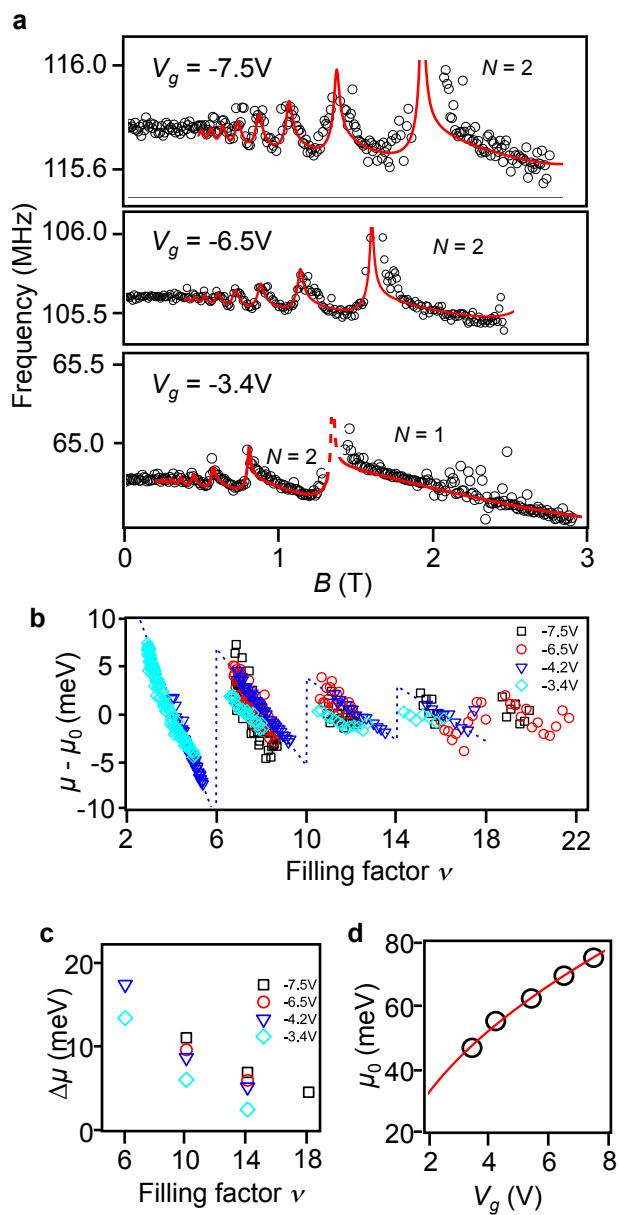
Supplementary Information

1 Electrical and mechanical characterizations of graphene resonators

Magneto-transport measurements are performed prior to mechanical resonance measurement. Fig. S1 also shows the two-terminal conductance G as a function of both gate voltage and applied perpendicular magnetic field, for device D2. Well-formed quantum Hall plateaus are observed. Typical contact resistances are $\simeq 5$ k$\Omega \cdot \mu$m, estimated from the two-terminal resistance at large carrier densities, and also from the deviation of the conductance from expected quantized values[1].
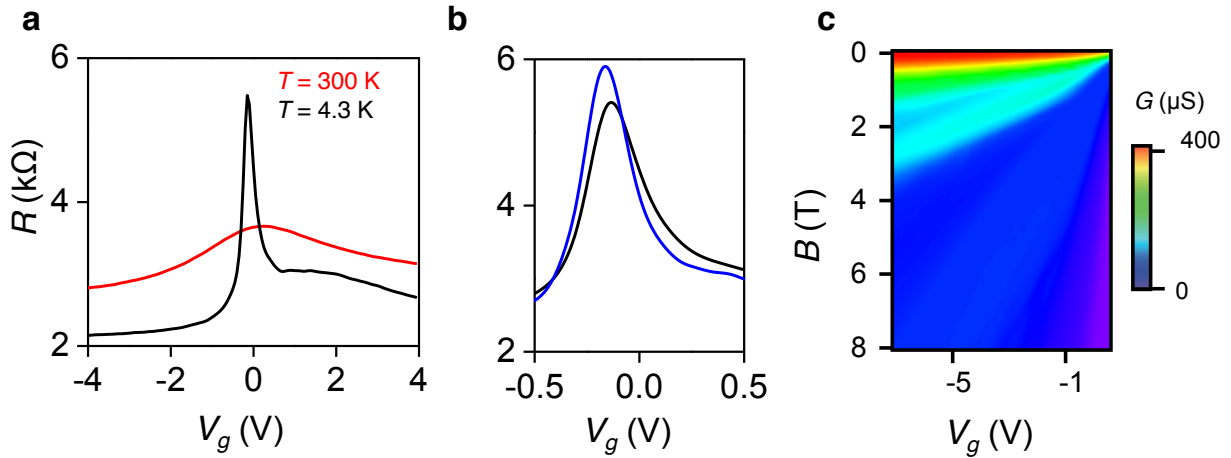

Figure S1 a. Resistance R of suspended graphene device D2 as a function of gate voltage V_g at 300 K and 4.3 K. Clear improvement of mobility is seen. b. Zoom-in of (a): Resistance R as a function of applied V_g before (black) and after (blue) current annealing. c. Two-terminal conductance G of D2 as a function of both gate voltage V_g and applied perpendicular magnetic field B.

For mechanical resonance measurements, the graphene membranes are electrostatically excited and detected using direct RF readout[2,3]. This technique, which uses the local gate to minimize stray capacitance, is two orders of magnitude faster than the commonly used heterodyne

mixing techniques[4,5] and enables quick characterization of device properties. In the meantime, the applied DC gate voltage V_g can tune the resonant frequency by electrostatically tensioning the sheet. Therefore, we measure the dependence of the resonant frequency f on V_g to identify devices with large tunability ($\Re_V = |\mathrm{d}f_0/\mathrm{d}V_g| \simeq 10$ MHz/V) resulting from low initial strain, which have the highest sensitivity to external forces.

Albeit quite robust, the direct RF readout method relies on finite $\mathrm{d}I_{sd}/\mathrm{d}V_g$ to transduce motion to the electrical domain, and typically a source-drain current of $I_{sd} \sim 10$ μA is required. Such large currents cause significant heating at low temperatures, particularly in the QH regime. Moreover, $\mathrm{d}I_{sd}/\mathrm{d}V_g$ vanishes on QH plateaus, making this measurement challenging. We overcome this issue by grounding the device ($I_{sd} = 0$) and using only the modulation of the gate capacitance to detect mechanical motion. The corresponding transmitted signal S_{21}, which is proportional to the vibration amplitude, is detected using a balanced bridge scheme to further reduce the parasitic capacitance[6,7]. Measurements are performed in ~ 10 mTorr He exchange gas, which is sufficient to cool the sample to base temperature without affecting the mechanical quality factor. The measured quality factor can be as high as $\sim 10,000$ with small driving power[5] (-80 to -60 dBm).
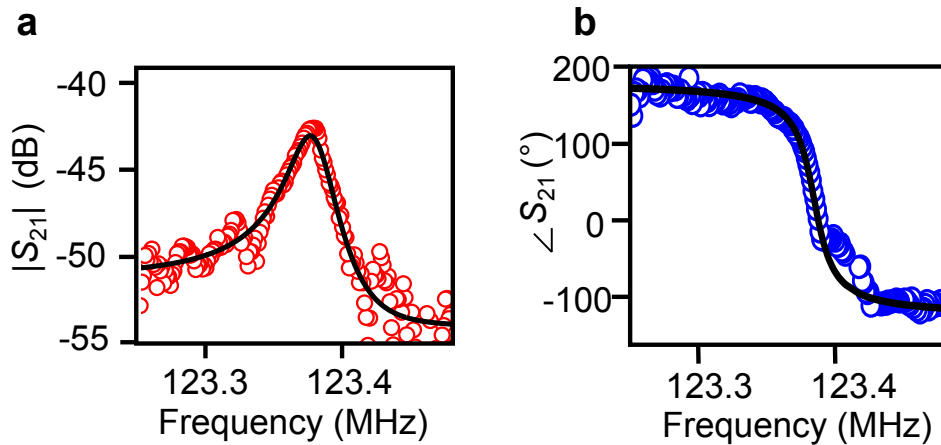

Figure S2 Measured S_{21} magnitude (a) and phase (b) for device D2 at zero magnetic field. The black curves are Lorentzian fits. Test conditions: T = 4.3 K, V_g = -4.2 V, drive

2

power is -68 dBm. The extracted quality factor is about 4700, and signal-to-noise ratio is 9.3 dB.

2 Mechanical Model of Graphene Resonators

We model the suspended graphene as a membrane with zero flexural rigidity[8] under a uniformly distributed force F (electrostatic force induced from applied DC gate voltage). Its fundamental vibrational mode is further treated in a 1D approximation, as that of a stretched string with a static deflection $\xi(x)$. Here, x is taken along the 1D string, and $\xi(x)$ is taken perpendicular to x, *i.e.*, perpendicular to the graphene membrane. The elastic energy stored in the stretched string U_{el} can be represented as[9]:

$$U_{el}[\xi(x)] = \int_0^L \frac{T}{2} \xi'^2(x) \mathrm{d}x = \int_0^L \left[\xi'^2(x) \left(\frac{T_0}{2} + \frac{ES}{4L} \int_0^L \xi'^2(u) \mathrm{d}u \right) \right] \mathrm{d}x, \qquad (1)$$

where E, S, and L are the Young's Modulus, cross-sectional area, length of the suspended graphene, respectively, and $\xi'(x) = \mathrm{d}\xi(x)/\mathrm{d}x$. We ignore the bending moment $EI\xi'^2(x)$ where I is the moment of inertia, since it is negligible in the case of single layer graphene, but can be significant for thicker membrane. Here I is the second moment of inertia. The two terms in the parentheses describe the total tension, $T = T_0 + T(V_g)$, which comes from both built-in tension $T_0 = \varepsilon_0 ES$ due to the fabrication, ε_0 is the corresponding built-in strain, and the induced tension $T(V_g) = \frac{ES}{2L} \int_0^L \xi'^2 \mathrm{d}x$ due to the elongation caused by the DC gate voltage V_g. Here the presence of V_g will also change the equilibrium position, *i.e.*, the exact form of $\xi(x)$.

The form of the static deflection in the case of 1D string under a uniformly distributed force is[8]

$$\xi(x) = zN(x) = z\frac{6}{L^2}(Lx - x^2), \qquad (2)$$

where $N(x)$ is normalized deflection function, and z is the effective displacement, such that $\int_0^L \xi(x)\mathrm{d}x = zL$. Then equation (1) becomes

$$U_{el} = \frac{12z^2}{L} \left(\frac{ES\varepsilon_0}{2} + \frac{3ESz^2}{L^2} \right). \qquad (3)$$
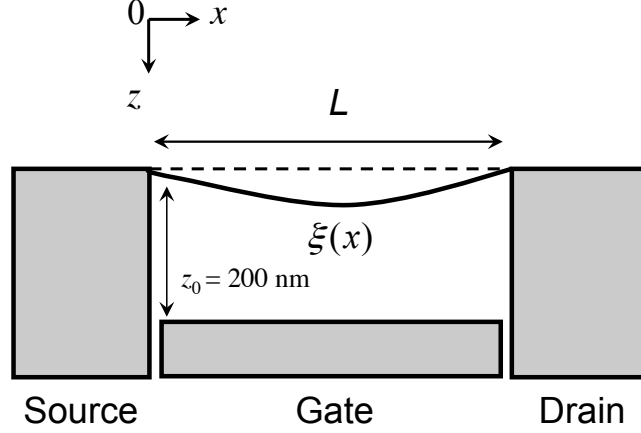
3

Figure S3   Schematics of the suspended graphene membrane as 1D string.

The suspended graphene can be treated as a metallic plate over the local gate electrode. Hence, the energy U_{es} stored in the capacitor is $\frac{1}{2}C_g V_g^2$, where C_g is the gate capacitance. We also need to consider the work done by the voltage source (battery) to keep the potential at V_g, which is $U_{batt} = -QV_g = -C_g V_g^2$. At zero magnetic field, the quantum capacitance is much larger than geometric capacitance, and can be ignored.

We next consider how the capacitance increases as the sheet is deflected toward the gate. We expand $C_g \approx C_0 + C_g' z + C_g'' z^2/2$, where $C_g' = \mathrm{d}C_g/\mathrm{d}z$, $C_g'' = \mathrm{d}^2 C_g/\mathrm{d}z^2$.

To determine the equilibrium position, we will consider the total energy, U_{total}, where

$$U_{total} = U_{el} + U_{es} + U_{batt}, \tag{4}$$

By taking the *total* derivative of total energy with respect to displacement, we obtain:

$$\frac{\mathrm{d}U_{total}}{\mathrm{d}z} = 0 = \alpha z^3 + \beta z + \zeta \tag{5}$$

where

$$\alpha = \frac{144ES}{L^3},$$

$$\beta = \frac{12ES\varepsilon_0}{L} - \frac{1}{2}C_g''V_g^2,$$

$$\zeta = -\frac{1}{2}C_g'V_g^2$$

The solution of (5), which gives the equilibrium mode shape $z_e N(x)$, is

$$z_e = -\frac{0.87\beta}{\sqrt[3]{9\alpha^2\zeta + 1.7\sqrt{4\alpha^3\beta^3 + 27\alpha^4\zeta^2}}} + \frac{\sqrt[3]{9\alpha^2\zeta + 1.7\sqrt{4\alpha^3\beta^3 + 27\alpha^4\zeta^2}}}{2.6\alpha}, \tag{6}$$

Using the actual device dimensions, typical built-in strain $\sim 0.1\,\%$, and a parallel plate model for the gate capacitance with gate-graphene separation of about 200 nm, we obtain $\alpha \sim 10^{15}$, $\beta \sim 10^0$, and $\zeta \sim 10^{-8}$, all with SI units, which prevent us from further simplify (6). These values give $z_e \sim 10$ nm for $|V_g| = 10$V.

The resonant frequency of the resonators f is:

$$f = \frac{\omega_0}{2\pi} = \frac{1}{2\pi}\sqrt{\frac{k_{\text{eff}}}{m_{\text{eff}}}}, \tag{7}$$

where ω_0 is the angular resonant frequency, k_{eff} is the effective spring constant and m_{eff} is the effective mass of graphene. If we assume the first vibrational mode is sinusoid, then for doubly clamped case, $m_{\text{eff}} = 0.5m_0$, where m_0 is the physical mass. In most cases, the effective mass will be larger than $0.5m_0$, due to the absorbed residue from fabrication.

Before we proceed, we will briefly discuss the effects of different forms of $\xi(x)$: if we assume the vibrational amplitude is much smaller than the static deflection $\xi(x)$, then the effective elastic restoring force acting on the graphene resonator can be written as:

$$\begin{aligned} F_{el} &= \frac{1}{L}\int_0^L \left[k\xi(x) + \tilde{\alpha}\xi^3(x)\right]\,\mathrm{d}x \\ &= kz + \tilde{\alpha}\frac{1}{L}\int_0^L \xi^3(x)\mathrm{d}x, \end{aligned} \tag{8}$$

5

where k is the linear spring constant, and $\tilde{\alpha}$ is the elastic nonlinear constant, and $\int_0^L \xi(x)\mathrm{d}x = zL$. Accordingly, the effective spring constant is:

$$k_{\text{eff},el} = k + 3\tilde{\alpha}\frac{1}{L}\int_0^L \xi^2(x)\mathrm{d}x. \tag{9}$$

If $\xi(x)$ is chosen such that it is independent of x, with $\xi(x) = z$, then $F_{el} = kz + \tilde{\alpha}z^3$, and $k_{\text{eff},el} = k + 3\tilde{\alpha}z^2$. This is just the simple point-mass-on-a-spring case. If $\xi(x)$ is chosen with the sinusoidal mode shape with $\xi(x) = z\frac{\pi}{2}\sin\frac{\pi}{L}x$, then $F_{el} = kz + \frac{\pi^2}{6}\tilde{\alpha}z^3$, and $k_{\text{eff},el} = k + \frac{3\pi^2}{8}\tilde{\alpha}z^2$. Finally, with our treatment of parabolic static mode shape, $F_{el} = kz + \frac{54}{35}\tilde{\alpha}z^3$, and $k_{\text{eff},el} = k + \frac{18}{5}\tilde{\alpha}z^2$.

From (5), the total effective spring constant k_{eff} is given as:

$$k_{\text{eff}} = \left.\frac{\mathrm{d}^2 U_{total}}{\mathrm{d}z^2}\right|_{z_e} = \frac{12ES\varepsilon_0}{L} + \frac{432ES}{L^3}z_e^2 - \frac{1}{2}C_g''V_g^2. \tag{10}$$

The first term in (10) determines the frequency of the graphene mechanical resonator at $V_g = 0$. The second term indicates the spring constant hardening due to the stretching: with increasing $|V_g|$, the suspended graphene is pulled more towards the gate, resulting a larger z_e, hence increase the spring constant. The last term is a spring constant softening, due to the non-linear nature of electrostatic force, and observed in other NEMS resonators[10,11]. For small ε_0, the second term dominates[4], and frequency increases monotonically with $|V_g|$. For large ε_0, the last term dominates[10], and frequency decreases with $|V_g|$. For intermediate ε_0, the resonant frequency first decreases, then increases, as V_g is increased[12]. Fig. S4 shows the simulated frequency tuning on the 2×2 $\mu\mathrm{m}^2$ graphene resonator, but with 200 nm gate-graphene separation (different from fig. 3 in main text), with different ε_0.
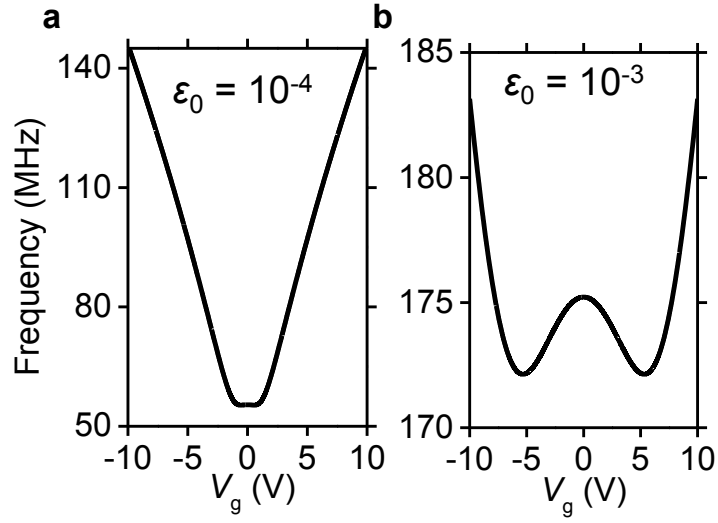
Figure S4 Simulated frequency tuning by V_g for a 2×2 μm^2 doubly clamped graphene resonator with 200 nm gap. a. with initial strain of 10^{-4} (0.01%) and b. with initial strain of 10^{-3} (0.1%).

    We can also applied this model to extract the initial strain and mass of the graphene from measured frequency tuning data, as shown in fig. S5. For device D2 shown in the main text, the initial strain is about 0.01%.
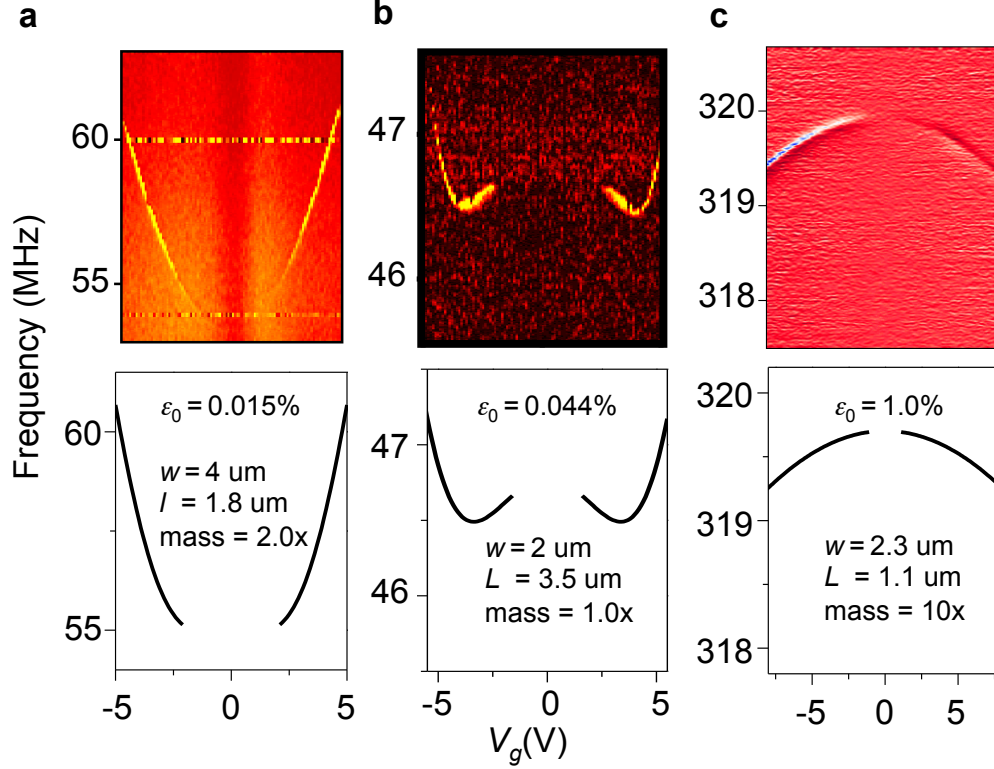
Figure S5 Top panel: resonant frequency of single layer graphene resonators as function of V_g, obtained from different devices. Bottom panel: fitted result with corresponding initial strains and mass (as multiples of pristine mass). The device dimensions are shown in the bottom panel as well.

However, in order for the frequency shift to be observed, it needs to be larger than the minimum resolvable frequency shift $\Delta f_{\min}$. In a mechanical resonator[13], $\Delta f_{\min}$ can be approximated as:

$$\Delta f_{\min} = 10^{-\frac{\text{SNR}}{20}} \sqrt{\frac{BW f_0}{2\pi Q}}, \tag{11}$$

where BW is the measurement bandwidth, f_0 is the resonant frequency, and Q is the quality factor. For graphene resonators, with f_0 in MHz range and $Q \approx 10000$ at low temperature, $\Delta f_{\min}$ is about few hundred Hz for reasonable BW. For a typical sample with mechanical resonance of 100 MHz, Q of 2000, and signal-to-noise ratio of 10 dB, in order to resolve 1 meV of chemical

potential variation from Δf_1 as described in main text, the minimum $\Re_V$ required is 5 MHz/V.

3   Mechanical Model of Graphene Resonators with Finite DOS

The above discussions treated graphene as prefect conductors, *i.e.*, with infinite carrier density of states (DOS). In reality, the finite DOS of graphene will modify the electrostatic and total potential energy. Here, we will consider it as perturbation of previous case.

With the presence of finite (and varying) DOS, as in our experimental settings, the carrier density n is no longer solely dependent of applied DC gate voltage V_g, but also determined by chemical potential μ. Their relation is implicitly defined by:

$$V_g = \frac{\mu}{e} + A\frac{ne}{C_g}, \tag{12}$$

where Ane/C_g represents the electrostatic potential, and A, e is the area of the suspended membrane and electron charge, respectively.

Total potential energy for DOS $\neq \infty$. Under such conditions, the electrochemcial energy stored in graphene is:

$$
\begin{aligned}
U_{ec} &= eA \int V_g \mathrm{d}\tilde{n} \\
&= eA \int_0^n \left(\frac{\mu}{e} + A\frac{\tilde{n}e}{C_g} \right) \mathrm{d}\tilde{n} \\
&= eA \left(\frac{\mu}{e}n + \frac{1}{2}\frac{Ae}{C_g}n^2 \right).
\end{aligned} \tag{13}
$$

When the membrane is deflected by different DC gate voltage V_g, all the n, μ, and C_g are modified, therefore, the accompanied force $\mathrm{d}U_{ec}/\mathrm{d}z$ is given as:

$$
\begin{aligned}
\frac{\mathrm{d}U_{ec}}{\mathrm{d}z} &= \left. \frac{\partial U_{ec}}{\partial n} \right|_{C_g,\mu} \frac{\mathrm{d}n}{\mathrm{d}z} + \left. \frac{\partial U_{ec}}{\partial C_g} \right|_{n,\mu} \frac{\mathrm{d}C_g}{\mathrm{d}z} + \left. \frac{\partial U_{ec}}{\partial \mu} \right|_{C_g,n} \frac{\mathrm{d}\mu}{\mathrm{d}z} \\
&= \left(A\mu + \frac{A^2 e^2 n}{C_g} \right) \frac{\mathrm{d}n}{\mathrm{d}z} - \frac{1}{2}\frac{A^2 e^2 n^2}{C_g^2} \frac{\mathrm{d}C_g}{\mathrm{d}z} + An\frac{\mathrm{d}\mu}{\mathrm{d}z}.
\end{aligned} \tag{14}
$$

9

Additionally, the applied DC gate voltage (electrochemical potential) is kept constant, and from equation (12), we have:

$$
\begin{aligned}
\frac{\mathrm{d}V_g}{\mathrm{d}z} &= \left.\frac{\partial V_g}{\partial n}\right|_{C_g,\mu} \frac{\mathrm{d}n}{\mathrm{d}z} + \left.\frac{\partial V_g}{\partial C_g}\right|_{n,\mu} \frac{\mathrm{d}C_g}{\mathrm{d}z} + \left.\frac{\partial V_g}{\partial \mu}\right|_{C_g,n} \frac{\mathrm{d}\mu}{\mathrm{d}z} \\
&= \frac{Ae}{C_g}\frac{\mathrm{d}n}{\mathrm{d}z} - \left(\frac{Ane}{C_g^2}\right)\frac{\mathrm{d}C_g}{\mathrm{d}z} + \frac{1}{e}\frac{\mathrm{d}\mu}{\mathrm{d}z} \\
&= 0.
\end{aligned}
\tag{15}
$$

By plugging equation (15) into equation (14), we are able to eliminate the $\mathrm{d}\mu/\mathrm{d}z$ term, and equation (14) is simplified to

$$
\frac{\mathrm{d}U_{ec}}{\mathrm{d}z} = A\mu\frac{\mathrm{d}n}{\mathrm{d}z} + \frac{1}{2}\frac{A^2e^2n^2}{C_g^2}\frac{\mathrm{d}C_g}{\mathrm{d}z}.
\tag{16}
$$

The presence of finite DOS does not change the expression for elastic energy U_{el}, which is same as equation (3). The work done the by the battery, U_{batt} can again be written as $U_{batt} = -V_g Aen$.

Taking the total derivative of all the three energy terms with respect to displacement z, we have:

$$
\frac{\mathrm{d}U_{total}}{\mathrm{d}z} = \frac{144ES}{L^3}z^3 + \frac{12ES\varepsilon_0}{L}z + (A\mu - V_gAe)\frac{\mathrm{d}n}{\mathrm{d}z} + \frac{1}{2}\frac{A^2e^2n^2}{C_g^2}\frac{\mathrm{d}C_g}{\mathrm{d}z}.
\tag{17}
$$

It is important to note there that, in the case of infinite DOS as discussed above, μ can be treated as zero, and if we further ignore the effects from C_g'', equation (17) will return to equation (5).

Force perturbation around equilibrium condition. Equation (17) reflects the total force F exerted on the graphene. Before proceeding, we can rewrite F as

$$
F_{el} = \quad = \frac{144ES}{L^3}z^3 + \frac{12ES\varepsilon_0}{L}z - \frac{1}{2}\left(V_g - \frac{\mu}{e}\right)^2\left(1 - 2\frac{C_g}{C_Q}\right)\frac{\mathrm{d}C_g}{\mathrm{d}z}
\tag{18}
$$

where $C_Q = Ae^2 (\mathrm{d}n/\mathrm{d}\mu)$ is commonly known as quantum capacitance, and $\mathrm{d}n/\mathrm{d}\mu$ is the DOS. In the derivation process, we again used the fact that $\mathrm{d}V_g/\mathrm{d}z = 0$ and chain rule.

At equilibrium, F is zero with the displacement of z_e, similar to the procedures that outlined for the infinite DOS situation. However, our interest here is how the presence of finite DOS will perturbate the force. When the magnetic field B is turned on, the graphene sample will go through different Landau levels (LLs), and undergo resulting variation of μ and C_Q (or equivalently, electronic compressibility). The force variation ΔF can be expressed as*:

$$\Delta F \approx - \left[\Delta\mu/e + C_g V_g \Delta \left(1/C_Q \right) \right] V_g \frac{\mathrm{d}C_g}{\mathrm{d}z}. \tag{19}$$

In equation (19), $\Delta\mu$ denotes the chemical variation, and $\delta(1/C_Q)$ represents the change in quantum capacitance (or compressibility) when B is swept through different LLs. The latter ($\delta(1/C_Q)$) is expected to be negligible except for cases between adjacent LLs.

Frequency shifts for $B \neq 0$. Next we will examine how the above force perturbation is translated to frequency shifts. Generically, the spring constant k can be expressed as:

$$k = \left. \frac{\mathrm{d}^2 U_{total}}{\mathrm{d}z^2} \right|_{z_e}, \tag{20}$$

with equilibrium displacement z_e. Now with the perturbation of magnetic field, the system will find a new minima of total potential energy, with new equilibrium displacement $\tilde{z}_e$. The new spring constant, $\tilde{k}$ can be written as:

$$
\begin{aligned}
\tilde{k} &= \left. \frac{\mathrm{d}^2 \left(U_{total} + \Delta U_{total} \right)}{\mathrm{d}z^2} \right|_{\tilde{z}_e} \\
&\approx \left. \frac{\mathrm{d}^2 U_{total}}{\mathrm{d}z^2} \right|_{z_e} + \left. \frac{\mathrm{d}^3 U_{total}}{\mathrm{d}z^3} \right|_{z_e} \Delta z_e + \left. \frac{\mathrm{d}^2 \Delta U_{total}}{\mathrm{d}z^2} \right|_{z_e} \\
&= k_0 - \left. \frac{\mathrm{d}k}{\mathrm{d}z} \right|_{z_e} \frac{\Delta F}{k_0} - \left. \frac{\mathrm{d}\Delta F}{\mathrm{d}z} \right|_{z_e} \\
&= k_0 + \Delta k_1 + \Delta k_2.
\end{aligned} \tag{21}
$$

*From hereon, the symbol Δ will denote the different between $B \neq 0$ and $B = 0$

In equation (21), we will further approximate $\mathrm{d}k/\mathrm{d}z$ with chain rule:

$$
\begin{aligned}
\frac{\mathrm{d}k}{\mathrm{d}z} &= \frac{\mathrm{d}k}{\mathrm{d}V_g}\frac{\mathrm{d}V_g}{\mathrm{d}F}\frac{\mathrm{d}F}{\mathrm{d}z} \\
&= \frac{\mathrm{d}k}{\mathrm{d}V_g}\frac{\mathrm{d}V_g}{\mathrm{d}F}(-k_0) \\
&\approx -\frac{\mathrm{d}k}{\mathrm{d}V_g}\frac{k_0}{V_g\frac{\mathrm{d}C_g}{\mathrm{d}z}}.
\end{aligned}
\tag{22}
$$

Finally, we arrive at the frequency shift $\Delta f = 0.5\Delta k\,(f_0/k_0)$ for $B \neq 0$ as:

$$
\Re_V \frac{\Delta F}{V_g\frac{\mathrm{d}C_g}{\mathrm{d}z}} = -\Re_V\left[\Delta\mu/e + C_g V_g \Delta\left(1/C_Q\right)\right]
\tag{23}
$$

where $\Re_V = |\mathrm{d}f/\mathrm{d}V_g|$, which is obtained from experiments.

Similarly, we can obtain Δf_3 as:

$$
\Delta f_3 \approx \frac{f_0}{2k_0}\left[\left(V_g\frac{\mathrm{d}C_g}{\mathrm{d}z}\right)^2\Delta\left(1/C_Q\right)\right].
\tag{24}
$$

4   Data Fitting

Geometric capacitance C_g**.** In order to determine the parameters for data fitting purpose, it is important to have accurate values of C_g. The observed frequency oscillation is periodic in $1/B$, and by performing same measurements at different V_g, we have found that the periodicity (in unit of T^{-1}) increase at decreasing $|V_g|$. Such periodicity is related to the cross-section of the Fermi surface[14], and in case of two-dimensional electron gas (2DEG), the periodicity in $1/B$ is given by[15]

$$
\Delta\left(\frac{1}{B}\right) = \frac{2e}{\hbar\pi n},
\tag{25}
$$

where $\hbar$ is the reduced Planck's constant. Fig. S6 shows the $1/B$ period vs. V_g, and the corresponding carrier density n according to equation (25). The geometric capacitance C_g is extracted

12

through:

$$C_g = Ae\frac{n}{V_g}. \tag{26}$$

To determine z_e and $\mathrm{d}C_g/\mathrm{d}z$, we use finite element analysis (COMSOL Multiphysics 4.2) to compute the capacitance at different values of z_e. We use the precise dimensions of the device, including fabrication imperfections (spike-like features at the edges of the local gate electrode), as shown in the inset of fig. S6. $\mathrm{d}C_g/\mathrm{d}z$ is then approximated as C_g/z_e.
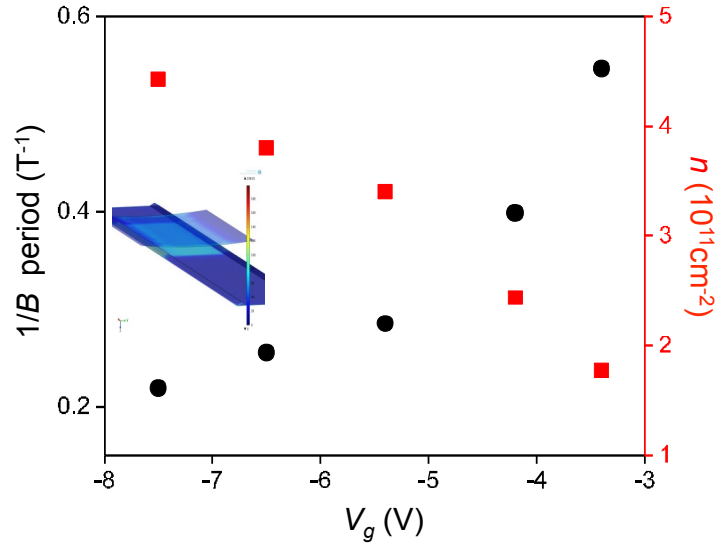

Figure S6 $1/B$ oscillation period and corresponding carrier density at different V_g. Inset: capacitance simulation with spike-like feature on local gate.

Frequency shifts for $B \neq 0$. The frequency tunability, $\Re_V$, is extracted from $B = 0$, as shown in fig. S7 for device D1 and D2.
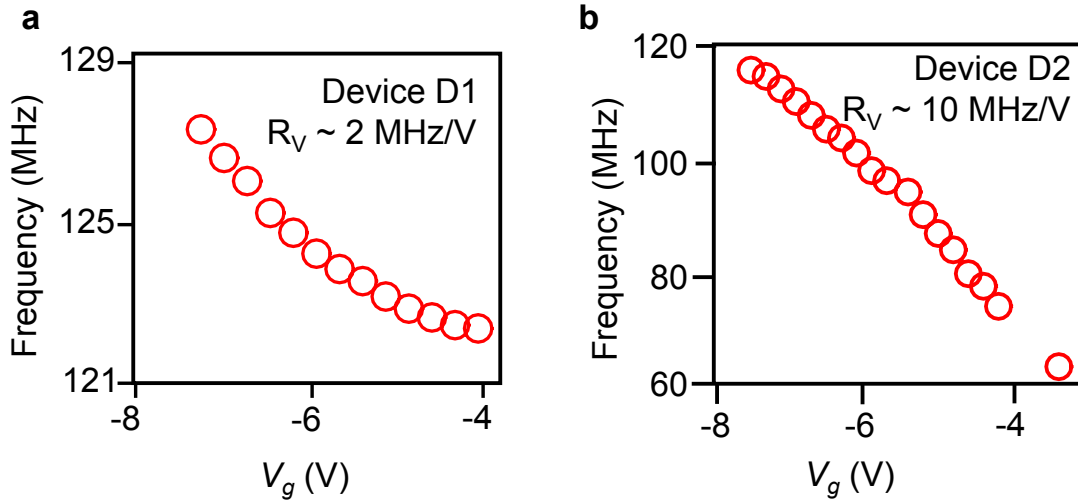
Figure S7 Voltage responsivities for device D1 and D2 at zero magnetic field.

As described in main text, we construct a simple DOS model consists of upto 20 LLs, each of which is Gaussian-broadened. The chemical potential at any given B and n is numerically determined as the highest energy level, and its evolution is shown schematically in fig. S8.

We therefore have obtained all information needed to perform the data fitting, with only LL broadening Γ as fitting parameter. The results are shown in main text, for different V_g. To obtain the best fit, Γ is slightly different for each V_g.
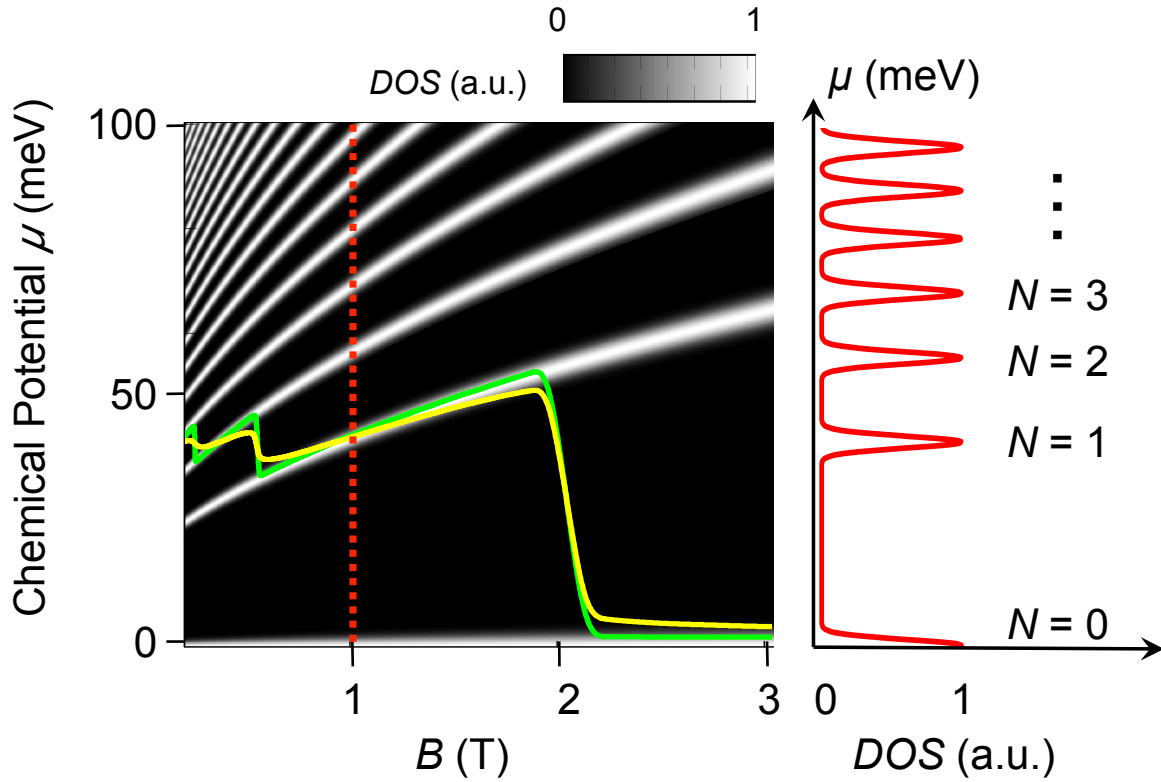
Figure S8 Exemplary DOS evolution as functions of both magnetic field B and chemical potential μ. The yellow and green traces on the left represent chemical potential μ oscillation (with respect to B) with different disorder strength, and the red trace on the right represent the chemical potential variation at $B = 1$ T, corresponding to the vertical dashed line on the left, showing the profiles of different LLs.

V_g (V)	1/B period (T^{-1})	n (10^{11}cm^{-2})	C_g (aF)	z_e (nm)	dC_g/dz (aF/nm)	f at B=0 (MHz)	k at B=0 (N/m)	μ at B=0 (meV)
-7.5	0.219	4.43	681	104.4	6.52	115.8	1.50	77.8
-6.5	0.255	3.81	668	103.3	6.47	105.6	1.27	72.1
-5.4	0.285	3.41	709	106.7	6.64	94.8	1.023	64.9
-4.2	0.398	2.42	638	100.5	6.35	75.3	0.636	57.7
-3.4	0.546	1.78	560	91.8	6.1	64.8	0.471	49.3

Figure S9 Summary of extracted parameters from experiments and COMSOL simulations (yellow shaded).

5 Signal detections between LLs

When the two-terminal graphene is positioned between adjacent LLs, the bulk of the sample becomes insulating, hence unable to carry mobile charges. The charges are conducted through the edges of the sample, resulting finite electrical resistance[16]. In such condition, the geometric capacitance C_g between graphene and the underlying gate is decreased due to the reduced effective lateral dimension, as well as the electrostatic force (fig. S10). For example, if the effective lateral dimension is reduced from 2μm to 52 nm (twice of magnetic length at $B = 1$ T, accounting for both edges), both the capacitance and capacitive force are dropped more than one order of magnitude. Additionally, the motional current also scales with C_g, therefore, the final measured signal will scale with C_g^2.

The diminishing electrostatic force and reduced signal transduction efficiency explain the vanishing of vibrational signal in regions between LLs, as shown in main text. Fig. S11 shows the vibrational amplitude, for $V_g = 7.5$ V, obtained from resonance fitting with Lorentzian line-shape. The minimum of vibration amplitudes correlate with the maximum of the resonant frequencies, consistent with our explanation. The smallest detectable amplitude is about 20% of the largest

value, indicating the geometric capacitance is reduced to about 44% of the parallel plate approximation. It is expected that the geometric capacitance will further decrease as the system approaches the center of the quantum Hall plateaus (middle of adjacent LLs), where current detection mechanism fails.
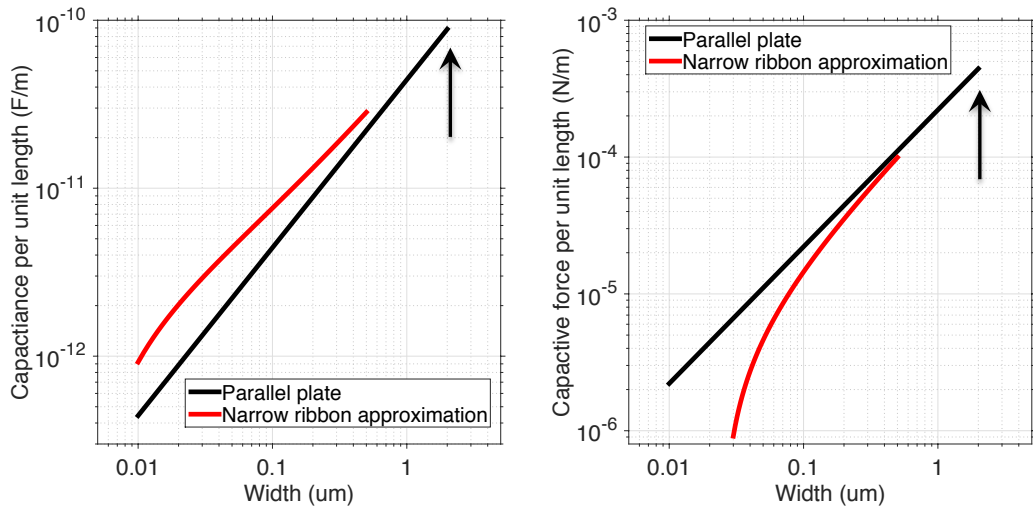

Figure S10   Capacitance and capacitive force with different lateral dimension, using both parallel plate formula and narrow ribbon over infinite plate approximation[17].
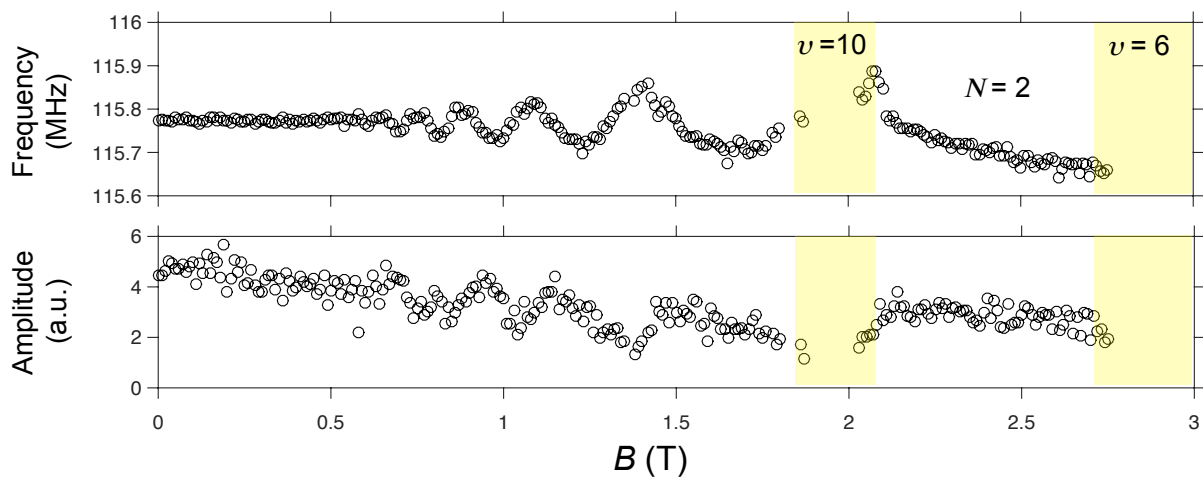
Figure S11 Resonant frequencies (top) and vibrational amplitudes (bottom) for V_g = -7.5 V.

The vanishing longitudinal conductivity σ_{xx}, will also decrease the RC charging rate. Although the two-terminal configuration prevents us from direct measurement of σ_{xx}, we estimate an lower bond for σ_{xx} of 10 nS, from measurements carried out in similar conditions[18]. It gives a worst-case-scenario estimation for RC charging rate of $\sim$ 10 MHz, well below the mechanical resonance $\sim$ 100 MHz. Therefore we cannot rule out effect from slow RC charging time, which will further contribute to the loss of signal.

1. Bolotin, K. *et al.* Ultrahigh electron mobility in suspended graphene. *Solid State Communications* **146**, 351–355 (2008).

2. Xu, Y. *et al.* Radio frequency electrical transduction of graphene mechanical resonators. *Appl. Phys. Lett.* **97**, 243111 (2010).

3. Lee, S. *et al.* Electrically integrated su-8 clamped graphene drum resonators for strain engineering. *Appl. Phys. Lett.* **102**, 153101–153101–4 (2013).

4. Chen, C. *et al.* Performance of monolayer graphene nanomechanical resonators with electrical readout. *Nature Nanotechnol.* **4**, 861–867 (2009).

5. Eichler, A. *et al.* Nonlinear damping in mechanical resonators made from carbon nanotubes and graphene. *Nature Nanotechnol.* **6**, 339–342 (2011).

6. Ekinci, K. L., Yang, Y. T., Huang, X. M. H. & Roukes, M. L. Balanced electronic detection of displacement in nanoelectromechanical systems. *Applied Physics Letters* **81**, 2253–2255 (2002).

7. Chen, C. *Graphene NanoElectroMechanical Resonators and Oscillators*. Ph.D. thesis, Columbia University (2013).

8. Weaver, W., Timoshenko, S. & Young, D. H. *Vibration problems in engineering* (Wiley-IEEE, 1990).

9. Sapmaz, S., Blanter, Y. M., Gurevich, L. & van der Zant, H. S. J. Carbon nanotubes as nanoelectromechanical systems. *Phys. Rev. B* **67**, 235414 (2003).

10. Wu, C. C. & Zhong, Z. Capacitive spring softening in single-walled carbon nanotube nanoelectromechanical resonators. *Nano Lett.* **11**, 1448–1451 (2011).

11. Kozinsky, I., Postma, H. W. C., Bargatin, I. & Roukes, M. L. Tuning nonlinearity, dynamic range, and frequency of nanomechanical resonators. *Applied Physics Letters* **88**, 253101 (2006).

12. Solanki, H. S. *et al.* Tuning mechanical modes and influence of charge screening in nanowire resonators. *Phys. Rev. B* **81**, 115459 (2010).

13. Ekinci, K. L. Ultimate limits to inertial mass sensing based upon nanoelectromechanical systems. *Journal of Applied Physics* **95**, 2682 (2004).

14. Onsager, L. Interpretation of the de haas-van alphen effect. *Philosophical Magazine* **43**, 1006–1008 (1952).

15. Kittel, C. *Introduction to Solid State Physics* (New York : Wiley, 1996).

16. Williams, J. R., Abanin, D. A., DiCarlo, L., Levitov, L. S. & Marcus, C. M. Quantum hall conductance of two-terminal graphene devices. *Phys Rev B* **80**, – (2009).

17. Batra, R. C., Porfiri, M. & Spinello, D. Electromechanical model of electrically actuated narrow microbeams. *Microelectromechanical Systems, Journal of* **15**, 1175–1189 (2006).

18. Zhao, Y., Cadden-Zimansky, P., Ghahari, F. & Kim, P. Magnetoresistance measurements of graphene at the charge neutrality point. *Physical review letters* **108**, 106804 (2012).